

A novel instrument to measure differential ablation of meteorite samples and proxies: The Meteoric Ablation Simulator (MASI)

D. L. Bones, J. C. Gómez Martín, C. J. Empson, J. D. Carrillo Sánchez, A. D. James, T. P. Conroy, and J. M. C. Plane

Citation: [Review of Scientific Instruments](#) **87**, 094504 (2016); doi: 10.1063/1.4962751

View online: <http://dx.doi.org/10.1063/1.4962751>

View Table of Contents: <http://scitation.aip.org/content/aip/journal/rsi/87/9?ver=pdfcov>

Published by the [AIP Publishing](#)

Articles you may be interested in

[Stardusts in Meteorites —Precursors of Planets](#)

AIP Conf. Proc. **847**, 319 (2006); 10.1063/1.2234419

[Supernova grains from meteorites](#)

AIP Conf. Proc. **402**, 287 (1997); 10.1063/1.53330

[Presolar material in meteorites: an overview](#)

AIP Conf. Proc. **402**, 3 (1997); 10.1063/1.53326

[Presolar oxide grains in meteorites](#)

AIP Conf. Proc. **402**, 59 (1997); 10.1063/1.53320

[Dust production in the galaxy: The meteorite perspective](#)

AIP Conf. Proc. **402**, 567 (1997); 10.1063/1.53319

PHYSICS
TODAY

**COMPLETELY
REDESIGNED!**



Physics Today Buyer's Guide
Search with a purpose.

A novel instrument to measure differential ablation of meteorite samples and proxies: The Meteoric Ablation Simulator (MASI)

D. L. Bones, J. C. Gómez Martín, C. J. Empson, J. D. Carrillo Sánchez, A. D. James, T. P. Conroy, and J. M. C. Plane^{a)}

School of Chemistry, University of Leeds, Woodhouse Lane, LS2 9JT Leeds, United Kingdom

(Received 9 June 2016; accepted 27 August 2016; published online 27 September 2016)

On entering the Earth's atmosphere, micrometeoroids partially or completely ablate, leaving behind layers of metallic atoms and ions. The relative concentration of the various metal layers is not well explained by current models of ablation. Furthermore, estimates of the total flux of cosmic dust and meteoroids entering the Earth's atmosphere vary over two orders of magnitude. To better constrain these estimates and to better model the metal layers in the mesosphere, an experimental Meteoric Ablation Simulator (MASI) has been developed. Interplanetary Dust Particle (IDP) analogs are subjected to temperature profiles simulating realistic entry heating, to ascertain the differential ablation of relevant metal species. MASI is the first ablation experiment capable of simulating detailed mass, velocity, and entry angle-specific temperature profiles whilst simultaneously tracking the resulting gas-phase ablation products in a time resolved manner. This enables the determination of elemental atmospheric entry yields which consider the mass and size distribution of IDPs. The instrument has also enabled the first direct measurements of differential ablation in a laboratory setting. © 2016 Author(s). All article content, except where otherwise noted, is licensed under a Creative Commons Attribution (CC BY) license (<http://creativecommons.org/licenses/by/4.0/>). [<http://dx.doi.org/10.1063/1.4962751>]

I. INTRODUCTION

The total flux of interplanetary dust particles (IDPs³⁶) entering the Earth's atmosphere has been measured by a variety of methods both within and outside the atmosphere, with estimates ranging between 5 and 240 t d⁻¹ (metric tonnes per day).¹ A major reason for this large uncertainty lies in the different assumptions required to interpret each type of measurement, which need to be corrected for different biases and involve a number of untested assumptions. Current efforts are being directed to reduce these uncertainties.^{2,3}

The major sources of IDPs are the asteroid belt, Jupiter family comets, Halley-type comets, and Oort cloud comets. In the Zodiacal Cloud Model (ZCM) developed by Nesvorný *et al.*,⁴ sub-millimeter particles from these sources are launched and tracked as their orbits evolve under the influence of solar radiation pressure, Poynting-Robertson drag, and planetary perturbations. Observations of infrared emission from the zodiacal cloud, measured by the Infrared Astronomical Satellite (IRAS), indicate that the majority (>80%) of the IR emission is produced by particles originating from Jupiter family comets.^{4,5}

The ZCM suggests that most of the IDP mass reaching the Earth is carried by particles in the 1–10 μg range, moving at an average velocity of 14 km s⁻¹. This ZCM estimates a total input of 41 t d⁻¹ (factor of 2 uncertainty). Radar observations, on the other hand, suggest that velocities are significantly faster (average = 30 km s⁻¹), which results in enhanced ablation and a lower input of ~5 t d⁻¹.⁶ These radar observations rely

on detecting the head echo of meteors, that is, the “ball” of electrons around the meteoroid that is produced by collisional ionization of the ablating metal atoms with air molecules. The mass and velocity of the IDP have to be estimated indirectly from the head echo signal. This is typical of observations of meteoric ablation: the ablation rates of the elements present in the IDPs must be inferred from radar head echoes, lidar observations,⁷ or from analysis of meteoric smoke particles in ice cores.^{8,9} Meteoric smoke is produced when the ablated metals form compounds (oxides, hydroxides, carbonates) which polymerize into nanoparticles which are most likely Fe–Mg–silicates.¹⁰ The interpretation of all of these observations requires an understanding of IDP ablation, atmospheric gas and aerosol chemistry of the resulting metals, transport and particle deposition.

To model the differential ablation of particles the Chemical Ablation Model (CABMOD) has been developed at Leeds.¹¹ This is based on a momentum and energy balance treatment of particles entering the atmosphere¹² and on the MAGMA code¹³ which calculates thermodynamic equilibria for the components in a silicate melt at high temperatures. CABMOD calculates the rate of heating and subsequent rate of ablation of the particle given the velocity, angle of entry, composition, density, and mass of an IDP. In calculating the rate of ablation, CABMOD assumes Langmuir evaporation by applying the Hertz-Knudsen relation: the atoms at the surface of the particle will ablate at a rate proportional to their equilibrium vapor pressure. The Langmuir coefficient is set to unity; that is, there is no energy barrier to evaporation. The melting of the particle is described empirically by a sigmoidal function, which allows for melting over a range of temperatures around

^{a)}J.M.C.Plane@leeds.ac.uk



the melting point of the particle.¹¹ This allows for the realistic scenario of partial melting below the melting point. Most of the melting occurs very near the specified melting point.

The Meteoric Ablation Simulator (MASI) has been developed to study meteoric ablation in the laboratory for the first time. The instrument is designed to test the various assumptions in a model like CABMOD: in particular, the melting and evaporation rates of the elemental constituents. IDP analogs (for example, ground-up meteorite particles) of radius 9–150 μm are heated to high temperatures (2900 K) in just a few seconds, thus mimicking their heating profiles during atmospheric entry. During this time the time-resolved ablation of the metallic constituents is detected by laser-induced fluorescence (LIF). From these measurements, it is possible to test both the thermodynamic model within CABMOD as well as the use of the Hertz-Knudsen relation to describe evaporation. Validation and refinement of CABMOD are desirable because the model is increasingly used for a variety of applications, including modelling meteor radar head echoes,¹⁴ calculating the Meteoric Input Functions (MIFs) of metals such as Na and Fe for whole atmosphere modelling,¹⁵ and interpreting the thermal histories of cosmic spherules.¹⁶ The first results on the ablation of Na, Fe, and Ca from meteoric analog particles using this apparatus are being published concurrently.¹⁷ This paper describes the MASI instrument itself.

II. EXPERIMENTAL SETUP

A. System description

The MASI consists of a heating filament mounted in a central vacuum chamber, pumped down to ~ 15 Pa. The chamber has 8 horizontal flanges as well as larger flanges at the top and the bottom of the chamber. These 10 ports allow (1) access to the filament, (2) the electrical feedthrough for the filament, (3) two detection lasers, and (4) perpendicular to them, 2 photomultiplier tubes, (5) a viewport for the pyrometer, and (6) an exhaust outlet (Figures 1 and 2).

The filament is a tungsten ribbon (Sigma Aldrich) 25 mm in length, 1 mm wide, and 0.025 mm thick. It is typically mounted so that there is a horizontal central portion on which the particles are placed (Figure 1(a)). The filament is mounted on the terminal block of an electrical feedthrough which is connected to a DC high-current/low-voltage power supply (Delta Elektronika ES 015-10). The currents used range from 0 to 8 A (0–3 V); at the maximum current, filament temperatures in excess of 2870 K are produced.

The stainless steel chamber is custom built (Lewvac Components Ltd.). The 8 horizontal viewports have 40CF conflat flanges whereas the ports at top and bottom are 63CF flanges. The filament feedthrough is attached via a QF flange for easy removal and re-attachment. The top flange allows either mounting of a second filament for calibration of the Fe laser signal or a window to view the sample directly or via a video camera. This window is removed to add a new sample to the filament. The chamber is pumped by an Edwards E2M28 rotary oil pump.

The filament temperature is measured with a rapid response pyrometer (System 4, R1 ratio thermometer, Land

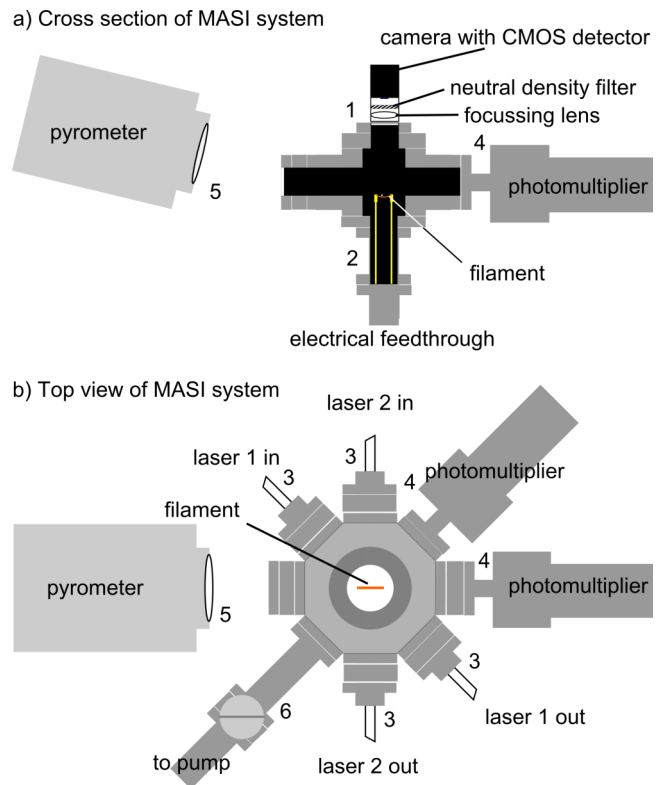


FIG. 1. Schematic diagram of the MASI. The pyrometer can also be mounted vertically above the chamber, with the video camera attached to its eyepiece. See text for key.

Instruments). This ratio pyrometer is capable of measuring the temperature of objects less than 1 mm wide with a stated time resolution of 15 ms. Its operating temperature range is 1273–2873 K, which is sufficient to recreate temperature profiles that IDPs (radius 9–150 μm) would experience upon entering the Earth's atmosphere at moderate velocities (14–31 km s^{-1}). Accurate temperature readings rely on the pyrometer being focused on the filament close to the point where the particles are located. The pyrometer calibration was checked by heating an iron filament to melting point (1811 K) and observing that the filament melted.

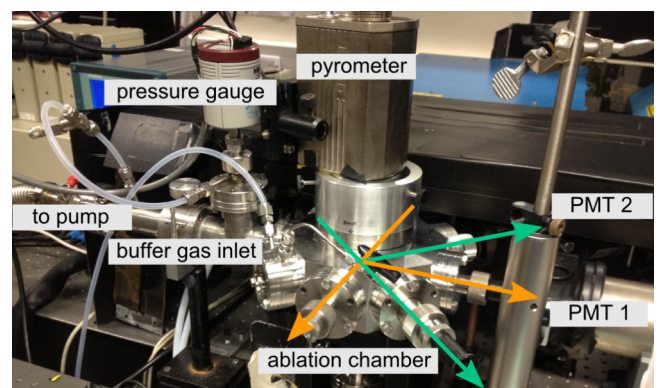


FIG. 2. Photograph of the MASI. The directions of the laser beams and the orthogonal fluorescence detection directions are highlighted in yellow (atomic Na LIF detection) and green (other metal atom LIF detection). All laser beams lie in the horizontal plane. In this setup, the pyrometer is mounted vertically above the MASI chamber.

TABLE I. Laser induced fluorescence settings for relevant elements.

Element	λ Nd:YAG (/nm)	Laser dye	λ_{\max} dye (/nm)	Doubling crystal	λ transition (/nm)	Transition
Na	532	Rhodamine 610	596		588.995	$3^2P_{1/2,3/2} \rightleftharpoons 3^2S_{1/2}$
Ca	355	Stilbene 420	425		422.673	$4^1P_1 \rightleftharpoons 4^1S_0$
Fe	355	Coumarin 503	500	BBO	248.327	$x^5F_0^o \rightleftharpoons a^5D_4$

Metal atoms ablated from the IDP analog particles are detected by fast time-resolved LIF. To date, the system has been configured to measure the ablation rates of Na, Fe, and Ca. In principle, the evaporation of any atom or oxide (e.g., SiO is predicted to be the major silicon species which ablates from metal silicates¹¹) can be observed so long as the species has a strongly allowed optical transition. Because Na is the most volatile of the meteoric metals and has an abundance $>0.1\%$ in a typical IDP analog,¹⁸ this is normally used as the reference and the *differential* ablation of the second metal with respect to Na is measured. Two tunable dye lasers (Cobra Sirah) are pumped at 250 Hz by the second and third harmonics of a single Nd-YAG laser (Litron, TRL 50-250). Table I contains the excitation/fluorescence wavelengths and appropriate laser dye for Na, Ca, and Fe. The resulting fluorescence is detected by high performance photomultiplier tubes (Electron Tubes, model 9816QB). Small monochromators (Edwards Minichrom, resolution 0.2 nm) set to the appropriate fluorescence wavelength are placed in front of the photomultipliers in order to discriminate against the broad black body radiation from the hot filament. In addition, the control system measures the background signal (from such sources as ambient light or emission from the filament) in between laser shots, which is then subtracted from the signal generated by the subsequent laser shot to leave the fluorescence signal. The use of a single Nd:YAG laser for pumping both dye lasers is crucial to having fully simultaneous measurements of the two species under study.

In order to record systematically the particle melting and any movement on the filament, a video camera was installed (a modified Microsoft LifeCam Cinema web cam). This camera has a CMOS detector with a maximum resolution of 1280×800 pixels at 25 Hz. The camera either utilizes the pyrometer optics, positioned behind the eyepiece of the pyrometer, or images the filament directly from above (port 1). Neutral den-

sity filters ($OD > 4$) were required to obtain an image of the filament at the higher temperatures. The camera is controlled by LabVIEW and is synchronized with the filament heating control loop.

B. MASI control system

The MASI control system carries out the following tasks: accurately reproduce the modelled meteoroid thermal profiles, trigger the laser pulses at 250 Hz, acquire the background-corrected LIF signal from the two photomultiplier tubes generated by each laser pulse, and relay the data to a control PC for display. The system operates at 500 Hz, allowing for collection of the background measurement between laser pulses.

The precise timing and substantial computational requirements of the MASI control system necessitate the use of a field-programmable gate array (FPGA) based controller. All time-critical control and data acquisition algorithms are implemented on a National Instruments CompactRIO 9075 controller using LabVIEW 2013 SP1. The FPGA running inside the CompactRIO controller has a 40 MHz clock, giving a time resolution of 25 ns. This temporal resolution is ample for the control system. A standard PC is used to run the host program with a user interface that communicates with the CompactRIO, initiating experimental runs and displaying and recording the data as they are acquired by the CompactRIO. The flow of signals and data in the control system is depicted in Figure 3.

Acquisition of data from the pyrometer and photomultiplier tubes is triggered simultaneously. The A/D conversion times of the I/O modules are closely matched; the NI 9203 module that measured the pyrometer temperature has a minimum conversion time $5 \mu\text{s}$, and the NI9215 module that acquired the voltage measurements from the photomultipliers has a conversion time of $4.4 \mu\text{s}$, so the measurement time

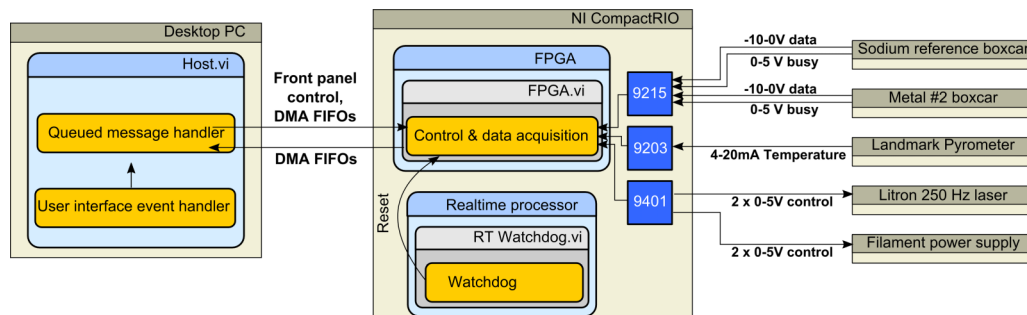


FIG. 3. The PC/CompactRIO/Instrumentation interface. Once the temperature control program is started, the FPGA on the CompactRIO processor receives and sends signals to the instruments on the right-hand side of the diagram, via the blue modules. The numbers in the blue boxes (9215, 9203, 9401) denote the National Instruments part number. The FPGA operates at 40 MHz.

difference is likely less than a microsecond, far slower than the experimental time resolution of 4 ms. The acquired data are forwarded to the control PC via a Direct Memory Access First In First Out (DMA FIFO) bus with metadata that ensure that the data can be reliably reconstructed. The LabVIEW software running on the PC receives the data, subtracts the background fluorescence measurements from the laser-induced fluorescence measurements, displays the data on the screen, and writes the data to disk.

Filament temperature control is achieved using a modified proportional, integral, differential (PID) control algorithm. Real-time temperature feedback is provided by the pyrometer. The time resolution achieved by operating at 500 Hz proved ample to control the filament temperature and match the target profile temperature. It is possible to reproduce heating and cooling rates as high as 2000 K s⁻¹ and -2000 K s⁻¹, respectively.

The current I supplied to the tungsten filament at time t is determined by the adapted PID algorithm

$$I(t) = K_p e(t) + K_i \int_0^t e(\tau) d\tau - K_d \frac{d}{dt} e(t),$$

where K_p , K_i , and K_d are the proportional, integral, and differential gain coefficients, respectively; the error term e is the desired filament temperature minus the actual temperature detected by the pyrometer and τ is the variable of integration, representing values of e at each time point.

The gain coefficients are tuned manually. The general procedure is as follows, and was repeated for low and high temperature set points: K_p was first increased until the temperature began to oscillate around the set point. The value of K_p was then reduced by around a quarter and K_i increased until the temperature began to overshoot. The value of K_i was then decreased by around a quarter and a small amount of K_d was applied as necessary to dampen the system response. The derivative portion of the controller was not always required, so in most cases the controller was run in PI mode.

C. Particle preparation

Particles for ablation are prepared by milling the mineral or meteorite of interest. The ground particles are then sorted into 5 size bins: 0–38 μm , 38–106 μm , 106–150 μm , 150–250 μm , and 250–355 μm with an Endecotts test sieve. This corresponds to effective average radii of 9, 36, 64, 100, and 150 μm , respectively. A range of meteorites are used as IDP analogs. The closest meteorites to IDPs are carbonaceous chondrites;¹⁹ however, ordinary chondrites are also useful analogs, not least because they are very abundant meteorites and easy to obtain. Meteoritic analogues are likely to be closer to the population of IDPs of asteroidal origin, which are more compact and contain some specific mineral assemblages. However, the mineralogy of C-type asteroids is not too dissimilar from that observed in cometary dust. IDPs sampled from the comet 81P/Wild2 by the Stardust spacecraft were seen to include olivine, feldspar, sulfides, and fine grained matrix material of CI composition, which can also be found in carbonaceous chondrites.²⁰ A further complication is that

cometary IDPs may be fragile aggregates that break up upon entering the Earth's atmosphere.²¹ This would result in a size distribution skewed towards the smaller particle sizes. However, while fragments of carbonaceous chondrite meteorites are only approximate analogs to IDPs, they are the closest available option.

Meteorites used in this work to obtain IDP analogs are Chergach (H5),²² Allende (CV3),²³ Murchison (CM2),²⁴ and NWA5515 (CK4).²⁵ A range of minerals known to be present in IDP are also considered (e.g., albite, labradorite, anorthite, forsterite, enstatite, and iron). The preparation and characterization of IDP analogs is explained in a separate concurrent publication.²⁶

D. Experimental procedure

The particles are suspended in a liquid such as ethanol. They can then be placed on the filament with a Pasteur pipette. The system is then isolated and gently pumped down to prevent the sample from falling off the filament. The solvent evaporates and only the solid mineral sample remains. A flow of nitrogen is added to maintain the pressure at 15 Pa.

The filament loading procedure takes patience and practice. With care, it is possible to load single particles, which can be confirmed with the video camera. Single particles of radius >50 μm produce detectable gas-phase metal atom concentrations. Below 50 μm (the smallest two size bins) loading typically results in many particles on the filament. These will correspondingly broaden the measured ablation pulses. This is partly due to the distribution of sizes and compositions within a given size bin for a given IDP analog. However, there will also be a contribution to the pulse width from coalescence and the resulting diffusion-limited ablation within the larger particles.

Once the operator is satisfied with the experimental setup parameters in the LabVIEW control software and starts the scan, the CompactRIO takes control of the system. Figure 4 is a flow chart of the events that occur once the experiment is started. The initial warm-up phase raises the filament temperature up to the lower detection limit of the pyrometer, 1273 K (1000 °C). To accommodate this experimental detection limit, the meteoroid thermal profiles are truncated to begin at 1273 K or higher. Evaporation of the metal species in the samples occurs at temperatures well in excess of 1273 K, so we do not believe that this limitation is detrimental to experiments measuring most of the major meteoric constituents (an exception would be sulfur). Upon reaching 1273 K the control system then transitions from the warm-up mode to the experimental mode in which the desired temperature profile is reproduced, simulating the temperatures experienced by a meteoroid during atmospheric entry. These profiles are prepared in advance and stored as text files that are loaded into the MASI control program. An example of a heating profile used in the MASI for a particle from the Chergach meteorite can be seen in Figure 5 in Section III. Further examples of heating profiles calculated in CABMOD for particles of different sizes and entry velocities are available in the [supplementary material](#) (Figures S1 and S2).

The pyrometer alignment is critical to the correct functioning of the control system. Even relatively small deviations

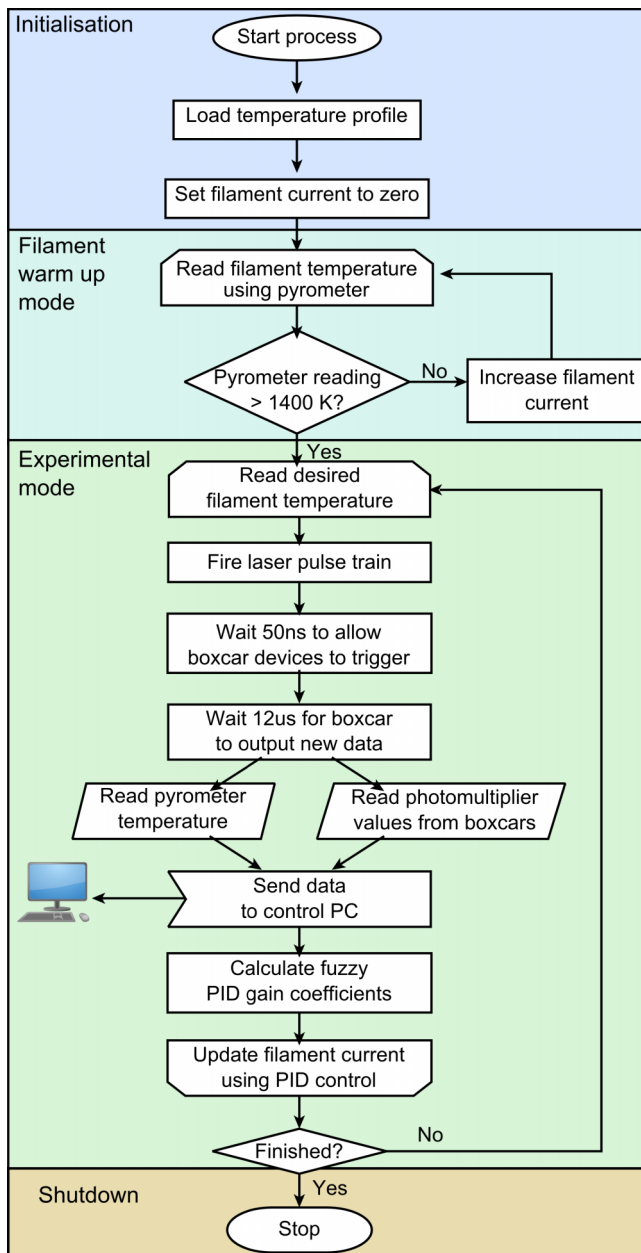


FIG. 4. Flow chart detailing the program control process performed by the FPGA on the CompactRIO during a scan.

from the correct alignment result in the pyrometer being unable to register a temperature reading until the filament reached temperatures well in excess of 1273 K. When this issue arises the PID controller quickly responds by reducing the current to the filament. The corresponding decrease in filament temperature coincides with the rapid increase in desired temperature, and the subsequent upward correction tends to overshoot, yielding a poor correspondence to the desired profile.

E. LIF signal calibration

The LIF signals for the pair of metals under study need to be calibrated with respect to each other in order to obtain a relative measure of the ablated metal concentration. Because of changes in laser performance and tuning, calibration needs

to be performed regularly. The mineral aegirine ($\text{NaFeSi}_2\text{O}_6$) was chosen to calibrate Fe with respect to Na, since it contains a 1:1 ratio of these elements. This was confirmed with Energy Dispersive X-ray spectroscopy (EDX). Repeat measurements of aegirine dust established the strengths of the Na and Fe LIF signals. Samples of the H5 Chergach meteorite have a 5:1 Fe to Na ratio, which was again confirmed by EDX. The calibration of the Ca LIF signal is more difficult due to the high melting point of calcium oxide in a melt. Labradorite (formula $(\text{Ca},\text{Na})(\text{Al},\text{Si})_4\text{O}_8$), is a potential calibrant but does not completely ablate when heated on the filament. In fact, the measured ratio from the EDX analysis of Chergach, which gives a 1:1 ratio of Ca to Na, means that Chergach dust can be used to calibrate the relative LIF signals.

F. Temperature profiles

In order to study the influence of particle morphology and composition on particle melting and evaporation, simple analytical temperature profiles such as linear ramps may be applied. These can then be used to convert the time axis into a temperature axis, allowing direct visualization of the temperatures of ablation onset, the peak ablation temperatures, and the full width half maximum (FWHM) of ablation pulses required for the benchmarking of CABMOD. To achieve full ablation of more refractory species such as Fe and Ca, linear profiles may be run several times, or high temperature step functions may be considered.

The atmospheric entry temperature profiles were calculated from the meteor physics module of CABMOD. Each profile requires the particle composition (based on the measured elemental abundance in the specific meteorite), density, radius, zenith angle, and velocity (see Figures S1 and S2 in the [supplementary material](#) for examples). The profiles of temperature as a function of time are then interpolated by a standalone LabVIEW program into the corresponding pyrometer current with a time resolution of 4 ms to match the resolution of the MASI. The maximum profile length (as prescribed by the size of the data bus on the FPGA) is 12 s or 3000 data points. Profiles of 8 s are commonly used for the meteoric profiles.

An assumption implicit in both CABMOD and the MASI experiments is that the particles are small enough to exhibit isothermal heating. Vondrak *et al.*¹¹ showed that this is the case for particles of radii less than 250 μm at temperatures below 2800 K, assuming that the particles are monocrystalline olivine. In cases where we have large particles of aggregate material these assumptions may not hold in either experiment or model. We have seen this to be the case occasionally for the largest particles in MASI. For both micrometeorites entering the atmosphere and IDP analogs on the MASI filament, the heating will be from one direction. Particles on the filament will only have a few direct points of contact with the filament, however, so the heating will not be as efficient. However, for particles less than 250 μm in radius the whole particle can be seen to melt in between successive camera frames; that is, in less than 40 ms.

Filaments typically last for 100 or so heating profiles before breaking. The filament lifetime can be extended by not overloading the filament with sample, not heating to the

maximum temperature, and by using shallow heating ramps. Eventually pronounced oscillations appear at higher temperatures; this is evidently feedback in the PID control system. This cannot be fixed by changing the PID settings, so it usually requires a change of filament. Filaments will break soon after the oscillations appear.

III. RESULTS

A. Evaporation of metal atoms from heated meteoric analogs

1. Temperature dependence of ablated metal atoms in the gas phase

Figure 5 shows an experimental simulation of ablation. The target temperature profile (green) matches closely the actual measured profile (red, dashed). The signals due to Na and Fe ablation (yellow and black lines, respectively) start to appear at around 1600 K. These are the raw signals from the photomultiplier tube, corrected for the background measurements between laser pulses. The Chergach meteorite particles on the filament have an average radius of $9\ \mu\text{m}$. The target profile has been calculated for a particle of this size entering the Earth's atmosphere at a velocity of $21\ \text{km s}^{-1}$. This results in a maximum temperature of around 2000 K, which is sufficient to ablate all of the Na and some of the Fe from these particles (Figure 5(a)). Subsequent repeat heating cycles of the filament ablate the remaining Fe (Figure 5(b)). In this case, all of the Fe has ablated 11 s into the scan. Typically it takes two repeat heating cycles to remove all remaining Fe. Using a small amount of sample helps minimize the residual metal on the filament.

Figure 6 compares the Na and Fe LIF signals for Al-lende meteorite particles of different sizes, exposed to a slowly ramping temperature profile. Apart from the Na signal for the smallest size bin (mean radius $9\ \mu\text{m}$), the Na starts to ablate at around 1650 K while the Fe does not ablate until 1800 K. This illustrates the phenomenon of differential ablation, which is the primary reason for the relative column abundances of the Na, Fe, Mg, and Ca layers in the upper mesosphere being far from the expected chondritic ratios.¹⁰ This is because Na (and K) ablates at lower temperatures and hence higher altitudes than Fe or even more refractory elements like Ca. The approximately 2 orders of magnitude depletion of the Ca layer with respect to Na is therefore explained because

a significant fraction of particles do not get hot enough to ablate Ca. The MASI system directly demonstrates this effect. Furthermore, the data from both linear ramps and realistic meteoric temperature profiles (such as in Figure 5) can be used to calculate differential ablation coefficients, based on the fraction of each element that is ablated from the meteor.¹⁷

2. Time response

In order to ablate a detectable concentration of metal from the particles, the pressure must be high enough to stop the metal diffusing straight to the walls of the chamber yet low enough to allow (i) the validity of the assumption of evaporation into a vacuum (which enables the use of the Hertz-Knudsen equation in the analysis of the data^{11,17}) and (ii) the rapid diffusion of the metal atoms into the detection region. Pressures of 15 Pa appeared to satisfy these requirements. Regarding evaporation, at 15 Pa the mean free path is $\sim 1\ \text{mm}$, much larger than the dimensions of the particles, which reduces the probability of a newly evaporated atom or molecule being “knocked back” into the melted particle surface. Moreover, assuming spherical diffusion from a constant finite source, the characteristic diffusion time (i.e., the time required to reach a steady state concentration) for Fe over the 3.5 cm distance to the detection point is around 20 ms²⁷ (diffusion coefficient D (Fe in N_2) = $85\ \text{cm}^2\ \text{s}^{-1}\ \text{Torr}^{28}$).

Figure S3 (supplementary material) shows the effect of the temperature dependence of the diffusion coefficient of Na in N_2 on the concentration at the detection point. The concentration difference is around 10% for average temperatures between the particle surface and the detection region between 500 K and 1500 K. However, the temperature measured 10 mm above the filament with a K-type thermocouple at the maximum filament surface temperature ($T = 2800\ \text{K}$) at 15 Pa is only 460 K, so the temperature dependence of the diffusion coefficient should have a negligible effect.

The rapid response of the concentration of metal to changes in the temperature of the particle can be clearly seen in experiments where an alternating current was applied to the filament (Figure 7). In these experiments, a solid state relay switch operating at 40-50 Hz connects the power supply with the tungsten filament in order to supply a square wave of alternating polarity. Rapid oscillations observed in the filament temperature are matched by equally rapid oscillations in the Na fluorescence signal.

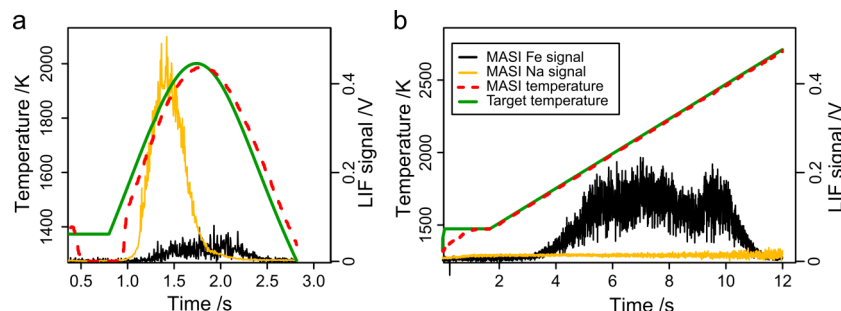


FIG. 5. An example of an atmospheric entry meteoric ablation simulation (panel (a)) and subsequent linear temperature ramp to remove any remaining material (panel (b)). The target temperature profile is shown in green. The actual measured profile in red matches this profile closely after an initial warm-up period. Sample: $9\ \mu\text{m}$ particles from the Chergach meteorite.

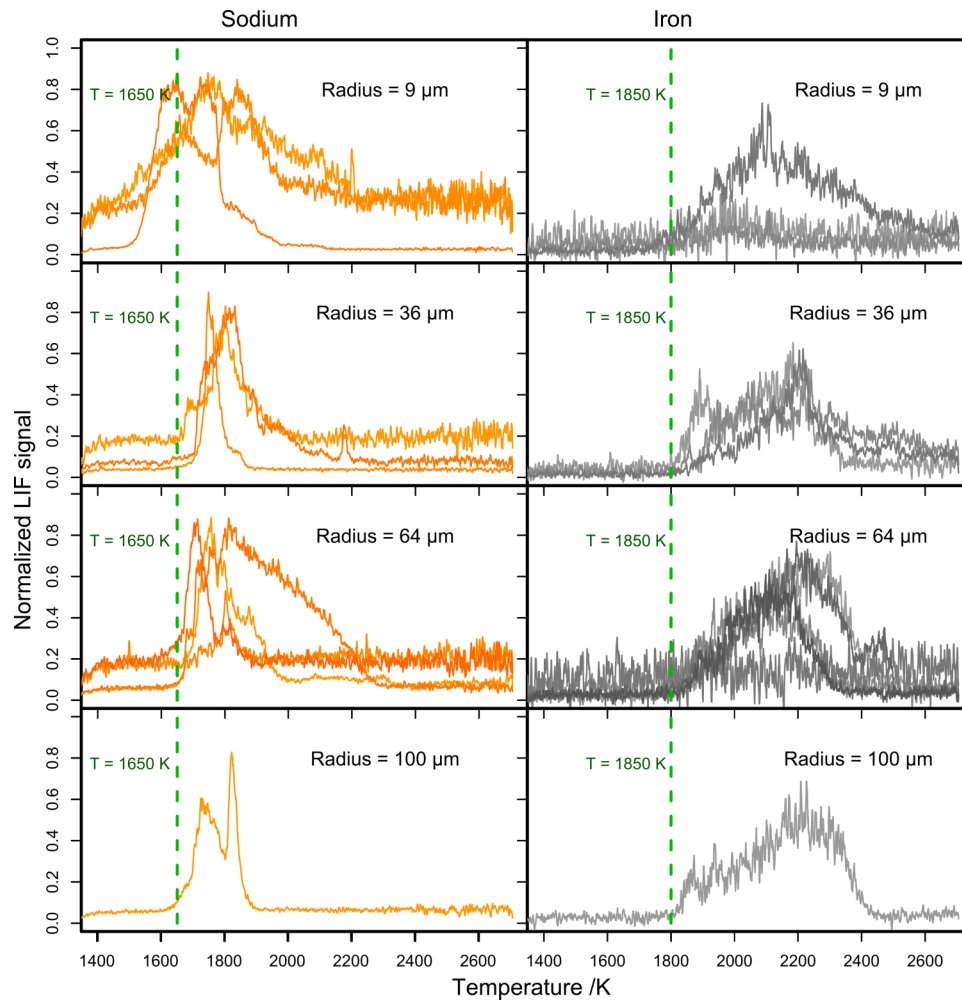


FIG. 6. A compilation of LIF profiles from linear heating ramps applied to particles from the Allende meteorite. Left hand side: Na LIF signal from four size bins: 9, 36, 64, and 100 μm average radius. Right hand side: The same four size bins for the Fe LIF signal. The x-axis has been presented as Temperature /K for Na and Fe (1650 K and 1800 K, respectively).

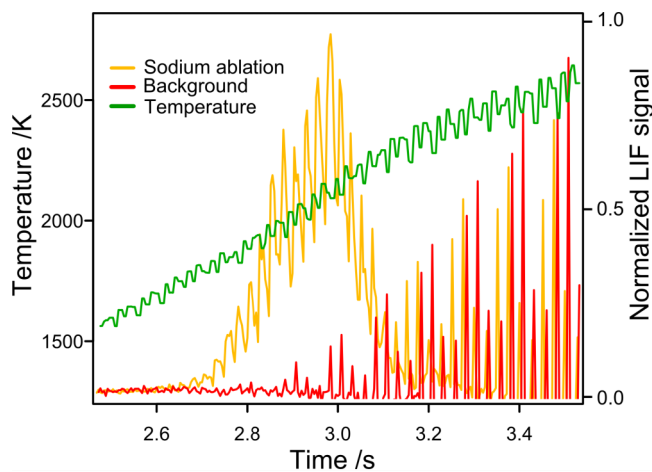


FIG. 7. Example of response of LIF signal and filament temperature to alternating current. The period of the oscillations of the Na LIF signal (yellow line) matches the period of oscillations of the temperature (green line). These are distinct from the background (red line) which only dominates at high temperatures.

Figure 7 compares the Na signal from a MASI run with an alternating current and a blank sample. In both cases, the oscillating background signal increases with temperature. Although the offline background measurement should be able to correct for background radiation, in this case it is not effective because the period of the applied alternating current is of the same magnitude as the sampling frequency. Therefore, a beating pattern can be observed in the background signal. In the signal from the sample, however, a clear Na LIF signal can also be seen. This also oscillates with the current as the temperature of the filament oscillates. Several observations can be noted: the Na LIF signal oscillation is due to ablation because it starts before the background signal dominates; the response of the ablation signal is faster than the period of the temperature oscillation, because the ablated products diffuse rapidly into the detection point; the measured temperature is out of phase with the LIF signal. Investigation of other MASI scans reveals that the measured temperature can lag behind the LIF signal by up to 20 ms, which is consistent with the stated 15 ms time response of the pyrometer.

Although the LIF measurement period of MASI is 4 ms, the time response of the pyrometer camera and the convolution

of signal by diffusion result in an effective time resolution of ~ 40 ms. An inspection of Fig. 6 shows that this is fast enough to obtain an accurate picture of the metal ablation profiles.

B. Melting of meteor analog particles

An unexpected observation is the tendency of molten particles to move along the filament. Particles will even move upwards, against gravity, from the lowest part of the filament. This effect complicates temperature measurements, since the pyrometer is focused near the initial position of the particles. If the particles move far from this location, the pyrometer temperature measurement may not reflect the temperature of the particles.

Furthermore, if the particles move through the pyrometer focus, there is an initial dip in the temperature profile followed by a spike as the filament temperature control program overcorrects before the particle moves out of the focus. The movement of the particles depends on the magnitude and direction of the current applied to the filament, suggesting that this is an example of the phenomenon of electromigration. In a solid, electromigration is caused by the transfer of momentum of electrons to the atoms in the conducting material and is typically against the current. In a liquid, however, the electrostatic force typically dominates and results in movement of the ions in the liquid with the current, towards the cathode.²⁹

When particles move to cooler parts of the filament, ablation of the more refractory elements (including Fe and Ca) can cease prematurely. Indeed, a glassy refractory residue was observed to build up at the ends of the filament over time. This does not interfere with ablation measurements since it is on a cooler part of the filament and all volatile species have already ablated. Where necessary, the filament can be manually heated to 3000 K to ensure this is the case.

As mentioned above, the MASI was modified at one stage to use an AC supply in an effort to prevent electromigration. In fact, there is a trade-off between using a high enough switching frequency to prevent the migration (and to minimize unwanted filament temperature fluctuations) and applying sufficiently long current pulses to heat the filament to the desired temperature. Moreover, using AC did not completely prevent electromigration. Two methods were used to supply AC power to the filament: manual control with a Variac and a pseudo alternating current from a square wave applied to a solid state relay. Neither method completely prevented migration and both methods resulted in unwanted oscillations of the filament temperature. The introduction of the AC supply also changed the electrical response of the filament: it drew a lower current, compensated by a higher voltage across it, and there was significant over- and under-shooting behavior as the control system attempted to reach the target temperature. The lag in the system was on the order of 0.2 s.

Attempts were also made to limit particle migration by roughening the surface of the filament. As the filament ages, the surface becomes rougher which inhibits migration to some extent. In some cases, the filament was pre-aged by exposing it to air at atmospheric pressure and moderate temperatures (~ 600 K). This does not significantly reduce electromigration.

Furthermore, such pre-aging further shortens the lifetime of the filament.

1. Particle tracking

The video camera was added to the system when it became clear that particles were moving unpredictably on the filament. It is important to know whether these particles are moving to cooler regions of the filament or ablating completely. LabVIEW programs were therefore developed to analyze the videos generated with the camera. Given that the width of the filament is 1 mm, it is straightforward to calibrate the distances on the videos. Once molten, particles appear brighter than the filament due to their higher emissivity and can hence be tracked as they move. The LabVIEW Vision Development module has many useful tools: with “IMAQ LineProfile” it is possible to extract the intensity profile along a chosen path in an image. When this path tracks a particle, the progress of the particle can be followed frame by frame as a peak in the intensity profile. As the current increases and the particle starts to move, its velocity and position change. If the particle ablates completely the peak in the intensity profile vanishes.

Figure 8 shows an example of particle tracking, corresponding to Na and Fe ablation events from particles of meteorite NWA5515 (radius ~ 64 μm). Two consecutive scans are presented in the main panel. The cartoon at the top of the diagram illustrates five events during the experiment. Panel 1 is a simplified version of Figure 9, for clarity. Panels 2–5 are simplified versions of later frames from the same video (see Videos S1(a) and S1(b) of the [supplementary material](#)). In the left-hand main panel the filament has been heating for 7.3 s, reaching a temperature (green solid line) of 2150 K before the Na (yellow solid line) ablates (NWA5515 has a higher melting point than Allende or Chergach). At this point, the filament is bright enough for particle tracking to commence. The particles do not start moving until about 10 s into the scan. The relative positions of 7 of the particles are shown by the purple lines. Two small particles coalesce with larger neighbors. As the particles start moving, Fe (black solid line) starts to ablate. 12 s into scan 1 (panel 3) three particles have ablated completely. This is the maximum length of time the FPGA can handle, so a second scan is started. Once the temperature is back to above 2100 K, the particles are molten, moving and ablating Fe. Of the four remaining particles, one ablates at 7.7 s (panel 4). By 9 s (panel 5) two particles have moved out of view while one ablates. The remaining two particles ablate off-screen.

Figure 10 is another example of particle tracking, this time observing Ca ablation events. The original snapshots and video corresponding to the cartoons are available in the [supplementary material](#) (Video S2). Here 4 particles (originally from a single large particle, Chergach meteorite, radius ~ 64 μm) are seen to move and ablate as the temperature (green line) increases linearly. At 6 s the Na (yellow line) has finished ablating. The particles start to move (position of each particle is depicted with the purple lines) whilst they (presumably) ablate Fe. The smallest particle ablates at 8.7 s (panel 1) releasing a small pulse of Ca (blue line). The next particle ablates at 9.4 s (panel 2) releasing another pulse of Ca. The final two particles

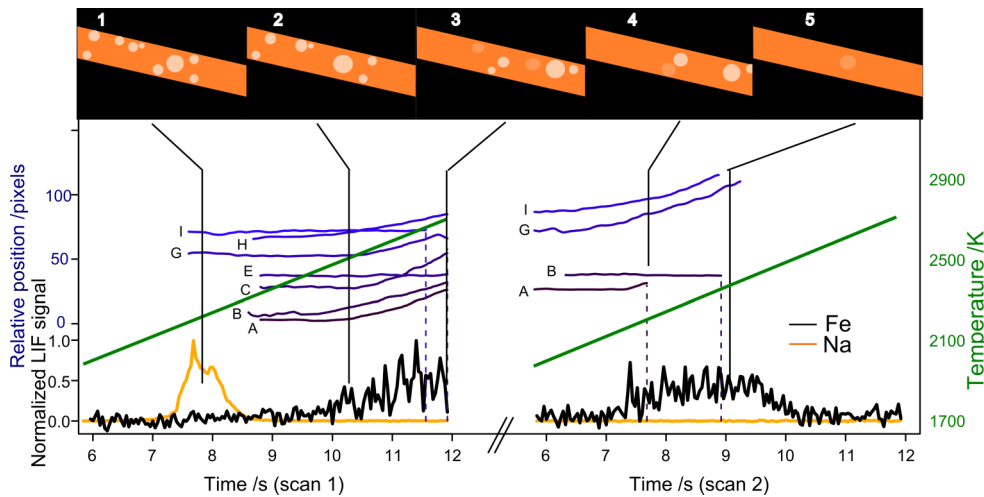


FIG. 8. Example of particle tracking. Two consecutive scans are presented here. The cartoon at the top of the diagram illustrates five events during the experiment. Panel 1 is a simplified version of Figure 9. Panels 2–5 are simplified versions of later frames from the same video (see Videos S1(a) and S1(b) of the [supplementary material](#)). Na signal: yellow line; Fe signal: black line; temperature: green line; relative particle positions: purple lines.

ablate at 10.2 s (panel 3), releasing a correspondingly large pulse of Ca.

If the pyrometer and camera are mounted vertically above the MASI chamber, with the camera located above the pyrometer, a useful view of the filament and reliable temperature measurements can be obtained. However, one issue with this arrangement is that the pyrometer target circle can be seen in the videos. It appears as a fuzzy black circle in the foreground which can complicate particle tracking. If the particles pass through the target circle, the measured temperature will dip, followed by an overcorrection from the heating control program.

2. Thermal gradient along the filament

The filament is usually hottest near the center; this is where the pyrometer is focused and where the particles are placed. It is necessary to characterize the temperature gradient as a function of distance along the filament in order to check that the movement due to electromigration does not expose the particles to unexpectedly high or low temperatures. Direct

measurements of the temperature with the pyrometer and temperatures determined from the intensity profile along the filament (using frames from videos of the filament) during heating events indicate that fresh, relatively flat filaments without deformations such as sharp bends or kinks have small temperature gradients within 3 mm of the center of the filament (Figure 11). The temperature gradient along the filament is unique to the particular filament. After the first couple of heating events, the temperature profile is relatively reproducible.

Figure 12 illustrates the filament temperature gradient along the length of the filament (in terms of the intensity of the light emitted by the filament and particle) during an experiment. The intensity profiles from subsequent video frames are plotted as a series of 2-D intensity profiles, with later frames appearing higher on the plot. This particular filament shows



FIG. 9. A frame 7.8 s into scan 1 of Figure 8, corresponding to Panel 1. See the [supplementary material](#) for the original video (SD).

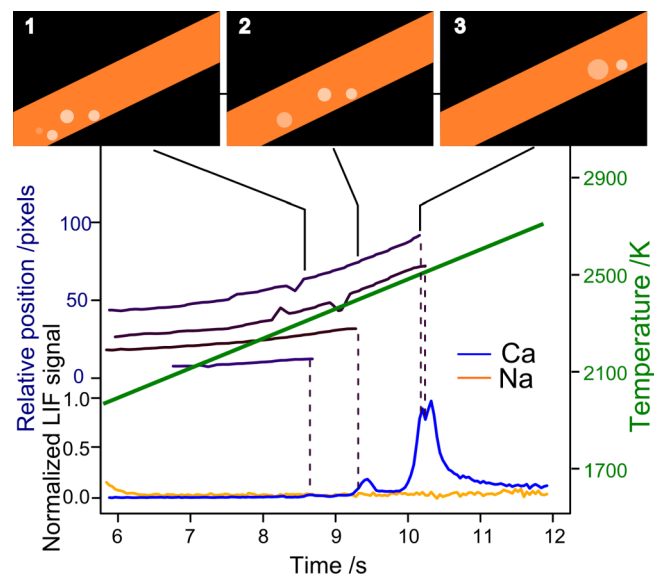


FIG. 10. Example of particle tracking. The cartoon at the top of the diagram illustrates three events during the experiment; the original frames from the video and the video itself are available in the [supplementary material](#) (Video S2). Na signal: yellow line; Ca signal: blue line; temperature: green line; relative particle positions: purple lines.

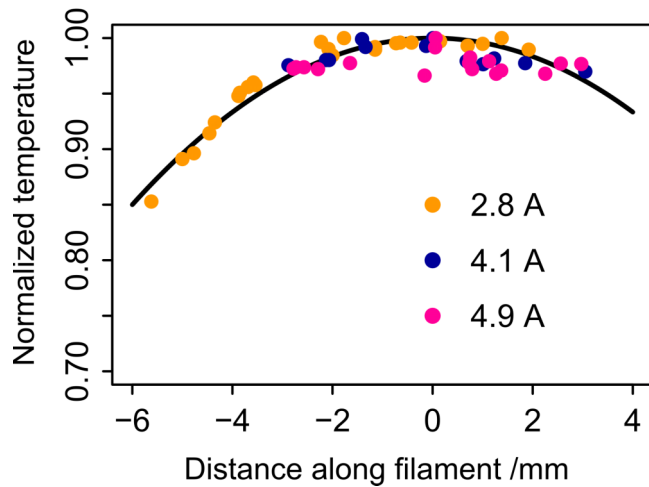


FIG. 11. The normalized temperature is plotted as a function of distance along the filament, with the center of the filament at 0 mm, for measurements at different currents (listed in the legend). Within 3 mm of the filament center, the temperature is essentially flat. A parabola (solid black line) has been added to guide the eye.

no significant temperature gradient as it is heated. The particle appears as a peak in intensity, seen to be moving to the right. Also visible are two dips representing the (black) pyrometer focus target circle.

3. Compositional dependence of particle movement

Videos of molten particles show clear differences in behavior between single phase systems (Fe_2O_3 , for example) and multiple phase systems such as meteorite samples. Single phase systems melt and then remain more or less in one place

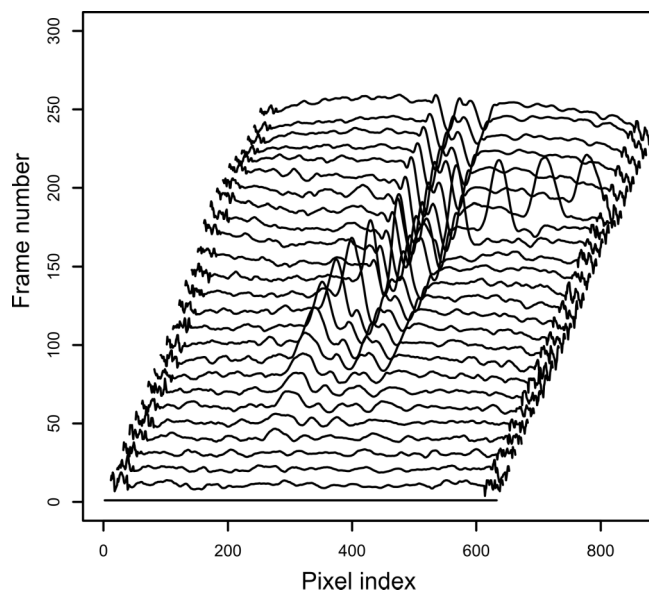


FIG. 12. The videos can be further analyzed frame-by-frame with the LabVIEW Vision modules. Here, intensity is plotted as a function of distance along the filament. Filament intensities are plotted for every tenth video frame (i.e., 0.4 s). As the particles melt, they appear brighter than the filament background and can be tracked. In this example the particle appears then moves to the right. The dips in intensity are due to the pyrometer target circle which becomes more pronounced as the filament gets brighter.

as they evaporate (Video S3 of the [supplementary material](#)). Multiple phase systems consist of a solid core of refractory material like calcium oxide in a molten pool of magnesium silicate (Video S4 of the [supplementary material](#)). It is these particles that exhibit the strongest electromigration effects; the particle can glide over the surface of the filament while still being held together by the surface tension of the components. This is advantageous: refractory compounds are held on the filament until they have a chance to melt and evaporate.

Aegirine ($\text{NaFeSi}_2\text{O}_6$) is an intermediate example: although it is a multi-component system, it is a relatively simple case with volatile components. Na and Fe evaporate at relatively low temperatures, leaving molten silicon dioxide. This often then spreads out rapidly to form a thin film on the filament before evaporating (Video S5 of the [supplementary material](#)).

4. Velocity as a function of current

Videos of the movement of particles on the filament during heating events were analyzed to determine how the velocity of the particle varied with current. Figure 13 plots the filament current against particle velocity for pyroxene particles. Above a current threshold of about 3.5 A in this case (corresponding to an experimental melting point of 2000 K) the particles start to move. Pyroxene, general formula $\text{XY}(\text{Si,Al})_2\text{O}_6$, where X is some mixture of Na, Ca, and Mg and Y is typically Fe^{3+} and Al, will exist as a multiple phase system at these temperatures. The higher the current, the greater the acceleration and hence the higher the final velocity. Very small particles (<0.1 mm molten diameter) and very large particles (1 mm molten diameter, i.e., the width of the filament) exhibit slower velocities than intermediate sized particles. Some of the scatter in Figure 13 will be due to the aging of the filament; older, rougher surfaces will inhibit electromigration to some extent.

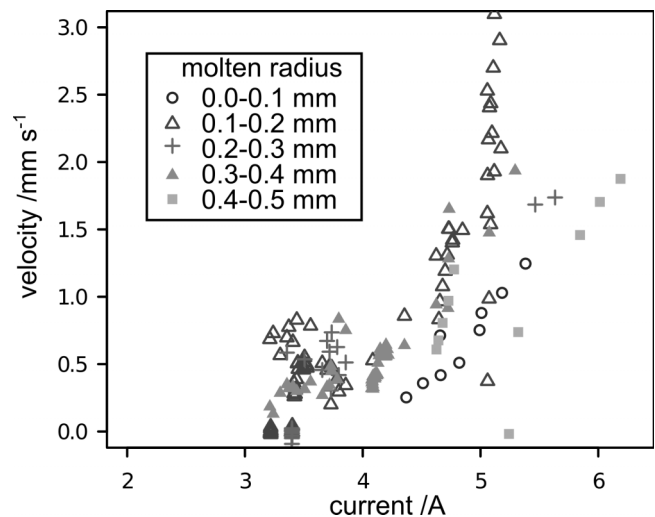


FIG. 13. Pyroxene particles (21 separate particles in total) are tracked as described in Section III B 1, enabling calculation of the velocity at each video frame. Here the velocity, averaged over 10 frames (0.4 s), is plotted as a function of applied current for particles of various sizes (radius, in mm). Distances and sizes can be calibrated from the known width of the filament (1 mm).

IV. DISCUSSION

A. Comparison to previous experiments

Previous experimental attempts to simulate the atmospheric ablation of meteoroids have focused on reproducing the atmospheric thermal processing deduced from micrometeorites retrieved on the ground, both from a textural and compositional perspective, in order to infer their origin.^{30–32} Recent experiments using pyrolysis and gas-phase infrared spectroscopy have also attempted to derive the yield of sulfur, CO₂, and H₂O in order to estimate the impact of micrometeoroids on planetary atmospheres.^{33,34} A new instrument has also been developed to measure impact ionization coefficients that can be potentially modified to study metal ablation.³⁵

The novelty of MASI with respect to these previous experiments is, firstly, the capability of prescribing and controlling with very high accuracy any shape of heating profile, including realistic atmospheric entry temperature curves obtained from momentum and energy balance equations.^{11,12} It should be noted that previous attempts of calculating elemental yields relied on unrealistic heating profiles and did not take into account the dependence of heating on particle size and entry speed.³⁴ A caveat is that the calculated entry profiles are essentially untested experimentally; they are obtained from the basic meteor physics equations, which make use of a number of uncertain parameters such as the free molecular drag coefficient and the free molecular heat transfer coefficient.¹¹ Charged particle accelerator experiments³⁵ may help to reduce the uncertainty of these parameters in the future. With the current understanding of differential ablation the use of mass and velocity dependent profiles is safer than applying a single artificial unrealistic heating profile.

Secondly, MASI is able to follow the temperature and elemental ablation rates of gas-phase species with very good time resolution (~40 ms, see Section III A 2). Previous experiments have only been able to measure total yields or residual fractions after applying temperature ramps. Thirdly, the use of LIF enables an extremely sensitive detection of the basic elemental constituents of IDPs. Besides Na, Fe, and Ca, other atoms such as Mg, K, Al, and Ni and molecules such as SiO are easily observable by atomic fluorescence.

B. Experimental limitations

MA SI is designed to measure the evaporation of moderately volatile and refractory elements, starting with Na and K. Phyllosilicates, very abundant in carbonaceous chondrites, will dehydrate to produce olivine below the temperature threshold of the pyrometer (1300 K), but this should also occur in the atmosphere within a similar time window (we maintain the system at the threshold temperature for about 2 s) and does not imply an evaporative loss of metallic species. The system cannot currently measure the ablation of more volatile species such as sulfur. For this, a pyrometer capable of covering the 600–1300 K range would be necessary. Also, because a fraction of sulfur evaporates as SO₂³⁴ other detection methods (e.g., FTIR) may be required in some cases. The system is sufficiently flexible to allow such changes.

The biggest experimental issue is the movement of molten particles due to electromigration. This has several undesirable effects: the temperature of the particles is not necessarily the same as the temperature measured by the pyrometer; particles move to cooler parts of the filament and do not ablate fully; and particles are more likely to coalesce. It does have benefits, however: the movement of the particles is composition dependent to a degree, so for meteoritic samples some evidence about the phases present in the melt can be obtained.

We have not yet found a means of preventing this particle movement. However, with the video camera installed we can at least measure the extent of the movement and note which scans exhibit complete ablation. We can also observe instances of coalescence as well as unusual melting behavior.

The upper temperature limit of MASI (2873 K) is dictated by both the temperature range of the pyrometer and this electromigration phenomenon. This means that we cannot simulate the entry of large (i.e., radius > 100 μm) and very fast particles (e.g., velocities above 30 km s⁻¹). A particle 150 μm in radius must be moving at speeds slower than 17 km s⁻¹ to have a peak temperature below 2800 K. Conversely, a particle moving at 41 km s⁻¹ needs to have a radius of 9 μm or smaller if the temperature is not to exceed 2800 K. In any case, the bulk of the particle size distribution in the ZCM is smaller than 100 μm in radius.

A more fundamental issue is with the compositional variation of the IDP analogs. While meteorites are reasonable proxies for IDP, attempts to mill meteorites into appropriately sized particles will result in particles of very varied composition and may result in biases with respect to size.²⁶ For example, an ordinary chondritic meteorite like Chergach comprises coarse grains embedded in a fine-grained matrix. The grinding process may leave the coarse grains intact, in which case they will only be present in the larger size bins. Even single particles can be heterogeneous and produce interesting behavior during heating: particles can disintegrate or actually explode into pieces as more volatile elements are released. The consequence of this intra- and inter-particle heterogeneity is that experiments must be repeated many times to build a representative data set.

Assuming these issues are recognized, it is possible to observe complete ablation for most elements expected in IDP. Hence, a detailed description of elemental ablation as a function of temperature can be developed in order to improve ablation models.

V. SUMMARY

This novel instrument enables us to measure evaporation of metals from meteorite samples or proxies in order to simulate experimentally the ablation of meteoric particles entering the atmosphere. The PID control of the filament temperature can reproduce modelled meteoric heating profiles to within 50 K, over a range from 1400 K to 2800 K.

An unexpected observation is movement of the particle due to electromigration. Various attempts to limit this effect proved partially successful at best. However, a video camera mounted on top of the chamber allows particle movement to be

tracked so that, if necessary, the temperature can be corrected to that corresponding to the actual position of the particle.

The MASI is now at a stage where the technique can be extended to investigate the ablation of further elements such as Mg and Si/SiO from meteorite samples. Data from the ablation of Na, Fe, and Ca have been used to update the meteoric ablation model CABMOD and will be published elsewhere.

SUPPLEMENTARY MATERIAL

See the [supplementary material](#) for videos of the experiments described in Figures 8 and 10 and Section III B 3.

ACKNOWLEDGMENTS

This work was supported by funding from the European Research Council (Project No. 291332 - CODITA).

- ¹J. M. C. Plane, *Chem. Soc. Rev.* **41**, 6507 (2012).
- ²J. D. Carrillo-Sánchez, J. M. C. Plane, W. Feng, D. Nesvorný, and D. Janches, *Geophys. Res. Lett.* **42**, 6518, doi:10.1002/2015GL065149 (2015).
- ³D. Janches, N. Swarnalingam, J. M. C. Plane, D. Nesvorný, W. Feng, D. Vokrouhlický, and M. J. Nicolls, *Astrophys. J.* **807**, 13 (2015).
- ⁴D. Nesvorný, P. Jenniskens, H. F. Levison, W. F. Bottke, D. Vokrouhlický, and M. Gounelle, *Astrophys. J.* **713**, 816 (2010).
- ⁵D. Nesvorný, D. Janches, D. Vokrouhlický, P. Pokorný, W. F. Bottke, and P. Jenniskens, *Astrophys. J.* **743**, 129 (2011).
- ⁶J. D. Mathews, D. Janches, D. D. Meisel, and Q. H. Zhou, *Geophys. Res. Lett.* **28**, 1929, doi:10.1029/2000GL012621 (2001).
- ⁷C. S. Gardner, A. Z. Liu, D. R. Marsh, W. H. Feng, and J. M. C. Plane, *J. Geophys. Res.: Space Phys.* **119**, 7870, doi:10.1002/2014JA020383 (2014).
- ⁸P. Gabrielli *et al.*, *Nature* **432**, 1011 (2004).
- ⁹L. Lanci, D. V. Kent, and P. E. Biscaye, *Geophys. Res. Lett.* **34**, L10803, doi:10.1029/2007GL029811 (2007).
- ¹⁰J. M. C. Plane, W. Feng, and E. C. M. Dawkins, *Chem. Rev.* **115**, 4497 (2015).
- ¹¹T. Vondrak, J. M. C. Plane, S. Broadley, and D. Janches, *Atmos. Chem. Phys.* **8**, 7015 (2008).
- ¹²S. G. Love and D. E. Brownlee, *Icarus* **89**, 26 (1991).
- ¹³B. Fegley and A. G. W. Cameron, *Earth Planet. Sci. Lett.* **82**, 207 (1987).
- ¹⁴D. Janches, L. P. Dyrud, S. L. Broadley, and J. M. C. Plane, *Geophys. Res. Lett.* **36**, L06101, doi:10.1029/2009GL037389 (2009).
- ¹⁵W. Feng, D. R. Marsh, M. P. Chipperfield, D. Janches, J. Hoeffner, F. Yi, and J. M. C. Plane, *J. Geophys. Res.: Atmos.* **118**, 9456, doi:10.1002/jgrd.50708 (2013).
- ¹⁶N. G. Rudraswami, M. S. Prasad, E. V. S. S. K. Babu, T. V. Kumar, W. Feng, and J. M. C. Plane, *Geochim. Cosmochim. Acta* **99**, 110 (2012).
- ¹⁷J. C. Gómez Martín, D. L. Bones, J. D. Carrillo-Sánchez, A. D. James, J. M. Trigo-Rodríguez, B. Fegley, and J. M. C. Plane, “Novel Experimental Simulations of the Atmospheric Injection of Meteoric Metals,” *Astrophys. J.* (submitted).
- ¹⁸K. Lodders and B. Fegley, *Chemistry of the Solar System* (Royal Society of Chemistry, Cambridge, UK, 2011).
- ¹⁹S. Taylor, G. Matrajt, and Y. B. Guan, *Meteorit. Planet. Sci.* **47**, 550 (2012).
- ²⁰M. E. Zolensky *et al.*, *Science* **314**, 1735 (2006).
- ²¹Y. Langevin *et al.*, *Icarus* **271**, 76 (2016).
- ²²M. K. Weisberg, C. Smith, G. Benedix, L. Folco, K. Righter, J. Zipfel, A. Yamaguchi, and H. C. Aoudjehane, *Meteorit. Planet. Sci.* **43**, 1551 (2008).
- ²³R. Clarke, E. Jarosevich, B. Mason, J. Nelen, M. Gomez, and J. R. Hyde, *Smithsonian Contributions to the Earth Sciences* (Smithsonian Institution Press, Washington, 1971).
- ²⁴L. H. Fuchs, E. Olsen, and K. J. Jensen, *Smithsonian Contributions to the Earth Sciences* (Smithsonian Institution Press, Washington, 1973).
- ²⁵M. K. Weisberg, C. Smith, G. Benedix, C. D. K. Herd, K. Righter, H. Haack, A. Yamaguchi, H. C. Aoudjehane, and J. N. Grossman, *Meteorit. Planet. Sci.* **44**, 1355 (2009).
- ²⁶A. D. James, V. L. F. Frankland, J. M. Trigo-Rodríguez, J. Alonso-Azcárate, J. C. Gómez-Martín, and J. M. C. Plane, “Synthesis and characterisation of analogues for interplanetary and meteoric material,” *J. Atmos. Sol.-Terr. Phys.* (to be published).
- ²⁷J. Crank, *The Mathematics of Diffusion* (Clarendon Press, Oxford, 1975).
- ²⁸D. E. Self and J. M. C. Plane, *Phys. Chem. Chem. Phys.* **5**, 1407 (2003).
- ²⁹P. Kumar, J. Howarth, and I. Dutta, *J. Appl. Phys.* **115**, 044915 (2014).
- ³⁰S. A. Sandford and J. P. Bradley, *Icarus* **82**, 146 (1989).
- ³¹A. Greshake, W. Klock, P. Arndt, M. Maetz, G. J. Flynn, S. Bajt, and A. Bischoff, *Meteorit. Planet. Sci.* **33**, 267 (1998).
- ³²A. Toppani, G. Libourel, C. Engrand, and M. Maurette, *Meteorit. Planet. Sci.* **36**, 1377 (2001).
- ³³R. W. Court and M. A. Sephton, *Geochim. Cosmochim. Acta* **73**, 3512 (2009).
- ³⁴R. W. Court and M. A. Sephton, *Geochim. Cosmochim. Acta* **75**, 1704 (2011).
- ³⁵E. Thomas, M. Horányi, D. Janches, T. Munsat, J. Simolka, and Z. Sternovsky, *Geophys. Res. Lett.* **43**, 3645–3652, doi:10.1002/2016GL068854 (2016).
- ³⁶Throughout this article, “interplanetary dust particle” will be used to refer to all dust particles in the zodiacal cloud, which become meteoroids when entering the Earth’s atmosphere.